Cell Reports

Article

Axon Growth of CNS Neurons in Three Dimensions Is Amoeboid and Independent of Adhesions

Graphical Abstract

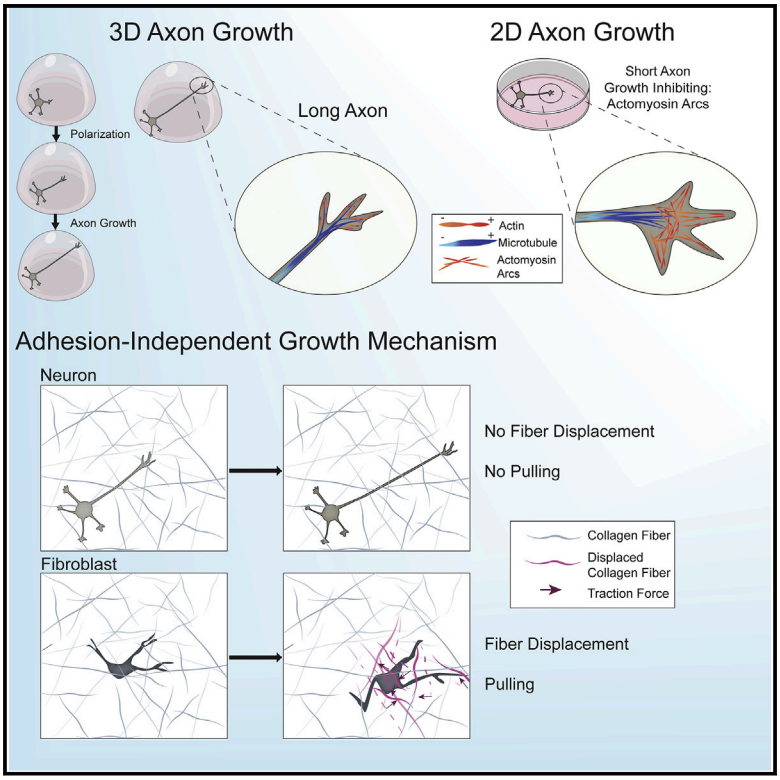

Highlights

- CNS neurons polarize and grow their axon in 3D similarly to *in situ*
- The axon grows in 3D unrestrained of actin filaments
- The axon extends without pulling on the extracellular matrix
- The growth cone does not need adhesion sites for axon extension in 3D

Authors

Telma E. Santos, Barbara Schaffran, Nicolas Broguière, Liane Meyn, Marcy Zenobi-Wong, Frank Bradke

Correspondence

frank.bradke@dzne.de

In Brief

Santos et al. show that embryonic CNS neurons can grow in an adhesion-independent manner in a 3D environment. Super-resolution and 3D-traction force microscopy show that CNS neurons grown in 3D polarize and grow their axon unrestrained from actin filaments and without pulling on the extracellular matrix.

Santos et al., 2020, Cell Reports *32*, 107907
July 21, 2020
https://doi.org/10.1016/j.celrep.2020.107907

CellPress

Cell Reports

CellPress
OPEN ACCESS

Article

Axon Growth of CNS Neurons in Three Dimensions Is Amoeboid and Independent of Adhesions

Telma E. Santos,[1,3,5] Barbara Schaffran,[1,5] Nicolas Broguière,[2,4] Liane Meyn,[1] Marcy Zenobi-Wong,[2] and Frank Bradke[1,6,*]

[1]Laboratory of Axon Growth and Regeneration, German Center for Neurodegenerative Diseases (DZNE), Venusberg-Campus 1, Building 99, 53127 Bonn, Germany

[2]Department of Health Sciences and Technology, ETH Zürich, Otto-Stern-Weg 7, 8093 Zürich, Switzerland

[3]Present address: Miltenyi Biotec B.V. & Co. KG, Friedrich-Ebert-Straße 68, 51429 Bergisch Gladbach, Germany

[4]Present address: EPFL SV IBI-SV UPLUT, AI 1112 (Bâtiment AI), Station 15, 1015 Lausanne, Switzerland

[5]These authors contributed equally

[6]Lead Contact

*Correspondence: frank.bradke@dzne.de

https://doi.org/10.1016/j.celrep.2020.107907

SUMMARY

During development of the central nervous system (CNS), neurons polarize and rapidly extend their axons to assemble neuronal circuits. The growth cone leads the axon to its target and drives axon growth. Here, we explored the mechanisms underlying axon growth in three dimensions. Live *in situ* imaging and super-resolution microscopy combined with pharmacological and molecular manipulations as well as biophysical force measurements revealed that growth cones extend CNS axons independent of pulling forces on their substrates and without the need for adhesions in three-dimensional (3D) environments. In 3D, microtubules grow unrestrained from the actomyosin cytoskeleton into the growth cone leading edge to enable rapid axon extension. Axons extend and polarize even in adhesion-inert matrices. Thus, CNS neurons use amoeboid mechanisms to drive axon growth. Together with our understanding that adult CNS axons regenerate by reactivating developmental processes, our findings illuminate how cytoskeletal manipulations enable axon regeneration in the adult CNS.

INTRODUCTION

During development, neurons polarize by generating an axon and a distinct somatodendritic compartment, the basic cellular properties required for neuronal circuitry (Schelski and Bradke, 2017). The axon emerges from the cell body led by the growth cone. The growth cone is the motile compartment for sensing guidance cues (Stoeckli, 2018) and contains the cellular machinery to drive axon outgrowth (Lowery and Van Vactor, 2009). The mechanism through which the growth cone drives axon growth in the central nervous system (CNS) is under intense investigation.

The structure of the growth cone and its cytoskeletal dynamics are closely associated with axon growth (Blanquie and Bradke, 2018). The central domain is microtubule rich and surrounded by actin filaments forming lamellipodia and filopodia in the peripheral fan-like domain (Forscher and Smith, 1988). Between these domains, actomyosin arcs form the transition zone, which may restrain dynamic microtubules from protruding into the peripheral domain (Dupraz et al., 2019; Schaefer et al., 2002). How cytoskeletal dynamics in the growth cone drive axon growth remains unclear.

Based on classical work in two-dimensional (2D) neuronal cell cultures, axon growth is thought to be mediated by the growth cone pulling itself and the trailing axon along the substrate by actomyosin-mediated contraction (Lin et al., 1994; Lowery and Van Vactor, 2009; Mitchison and Kirschner, 1988). In this model, cell adhesions act as a molecular clutch by anchoring actin filaments. Thereby, the anchored actin filaments reduce retrograde flow, resulting in actin-based forward protrusion of the growth cone (Jay, 2000; Short et al., 2016). CNS neurons, however, can still extend their axons on 2D substrates upon actin depolymerization (Bradke and Dotti, 1999; Kunda et al., 2001) or inactivation of myosin II (Dupraz et al., 2019; Neukirchen and Bradke, 2011; Rösner et al., 2007). Moreover, neurons can extend axons in liquid medium (Letourneau et al., 1987). Thus, the growth mechanism underlying axon extension has remained unclear.

We investigated the underlying mechanisms of axon growth and growth cone motility in three-dimensional (3D) matrices. These matrices provide a more physiological environment compared to 2D cultures yet still enable the investigation of single cells without cell-cell interactions. We show that neurons extend axons independent of pulling and without the need of adhesions in 3D environments. In contrast to their dynamics in 2D environments, in 3D, microtubules grew unrestrained from the actomyosin cytoskeleton into the growth cone leading edge to enable rapid axon extension (Lowery and Van Vactor, 2009). Together, these data demonstrate that developmental axon growth is amoeboid and challenges the physiological importance of force-based mechanisms in the CNS. As axon growth

is the key step in regrowing a lesioned axon, these data provide a mechanistic concept to elicit axon regeneration by reigniting amoeboid growth after injury.

RESULTS

Embryonic Hippocampal Neurons in 3D Polarize Rapidly Recapitulating Growth Patterns *In Situ*

To investigate the mechanisms underlying axon growth in 3D, we encapsulated dissociated mouse embryonic hippocampal neurons (Kaech and Banker, 2006) in collagen matrices. Fixation and imaging of neurons showed that neurons grown in collagen matrices developed faster than neurons grown on 2D poly-L-lysine (PLL) or 2D collagen. Specifically, neurons cultured in 3D extended their neurites more rapidly (Figures 1A and 1B). By 24 h, axons in 3D had reached an average longest neurite length of 64 ± 2 μm (mean ± SEM; Figure 1B), doubling the lengths of neurons grown on 2D PLL or collagen (Figures 1A and 1B). Furthermore, hippocampal neurons polarized faster in 3D than in 2D. After 12 h, 90% of neurons formed neurites (stage 2) or even an axon (stage 3), whereas in 2D, almost 40% of neurons had remained spherical (stage 1) (Figures 1C and 1D). Consistently, by 24 h, the proportion of 3D-cultured neurons with a Tau-1-positive (Tau-1^{+}) axon doubled compared to neurons grown on 2D substrates (Figures S1A and S1B). The number of neurites was not affected by the 3D environment, and the total neurite length tended to increase in 3D (Figures S1C and S1D). Notably, time-lapse differential interference contrast (DIC) microscopy revealed that neurites in 3D were more dynamic than neurites on 2D PLL or collagen (Figures 1E and 1F; Video S1). Specifically, the speed, frequency, and length of extension and retraction events increased in 3D compared to both 2D conditions. We observed similar dynamic growth patterns in neurons grown in hyaluronic acid (HA) matrices (Figures S1E and S1F; Video S2), the major component of the CNS extracellular matrix (Ruoslahti, 1996). To further delineate axon growth dynamics in more physiological conditions, we labeled hippocampal neurons in the developing mouse hippocampus by *in utero* electroporation. Time-lapse imaging of *ex vivo* hippocampal slices revealed a similar growth pattern as observed in 3D collagen and 3D HA matrices (Figures S1E and S1F; Video S2). Thus, axon growth dynamics in 3D matrices are similar to that observed in physiological conditions but differ from the slower axon growth found in 2D cell cultures.

Microtubules Reach the Growth Cone Leading Edge in 3D

As the growth cone contains the machinery for axon growth (Gomez and Letourneau, 2014), we investigated growth cone dynamics and changes in the underlying cytoskeleton. Time-lapse DIC microscopy revealed that the dynamic growth cone area was doubled in size in collagen matrices compared to 2D conditions (Figures 2A and 2B; Video S3). Interestingly, the cytoskeletal arrangement substantially differed in 3D growth cones compared to growth cones in 2D. Stimulated emission depletion (STED) microscopy depicted the well-known structure of growth cones in 2D (Figures 2C and 2D), with the central domain enriched in microtubules, surrounded by filopodia and lamellipodia in the peripheral domain; actin arcs define the transition domain. By contrast, growth cones observed in 3D lacked partitioning into distinct domains (Figures 2C and 2D). Instead, we detected an actin-rich area containing filopodia devoid of actin arcs and lamellipodia (Figures 2C and 2D; Video S3).

To investigate the cytoskeletal dynamics in growth cones of neurons in 3D matrices, we performed time-lapse microscopy of neurons transfected with markers for the dynamic cytoskeleton. In growth cones of neurons expressing fluorescently tagged plus-end-binding protein 3 (EB3-mNeonGreen) and Lifeact (Lifeact-RFPruby), which label polymerizing microtubules and actin filaments, respectively (Figure 2E), we found comparable actin retrograde flow and microtubule growth speed in 2D and 3D (Figures 2F and 2G). Importantly, however, microtubule ends protruded closer to the leading edge in growth cones of neurons cultured in 3D collagen (Figures 2E and 2H; Video S3). Could the microtubules be less restricted in their growth in 3D, thereby enabling more rapid axon growth?

The Actomyosin Network Restrains Axon Growth in 2D

As microtubules were able to reach the growth cone leading edge in 3D, but not in 2D, we hypothesized that in 2D, axon growth is restrained by actomyosin arcs in the transition zone, where they prevent microtubule advance (Figure 3A). To test this hypothesis, we treated neurons with the actin depolymerizing drug cytochalasin D or the myosin II inhibitor blebbistatin. Indeed, we found that both treatments of neurons grown on 2D substrates enhanced axon outgrowth to lengths similar to those of neurons grown in 3D (Figures 3B and 3C). Importantly, neurons cultured in 3D showed no additional growth upon either treatment. Thus, axon growth in 2D, but not in 3D, is promoted by actin destabilization or relaxation of the actomyosin network (Figure 3D). It suggests that the actomyosin cytoskeleton plays a less important role in axon growth in 3D than previously anticipated.

Axons Grow without Pulling on the 3D Matrix

Given that inhibition of the actomyosin system does not prevent neurons in 3D from growing their axons, we hypothesized that axons can extend without pulling on the matrix. To test this, we assessed contraction of collagen gels containing developing neurons. In contrast to fibroblasts, which are well known to migrate by pulling on their surroundings (Tomasek et al., 1992), we found that neurons did not exert any measurable force on the collagen gel (Figures 4A and 4B). We therefore directly assessed growth cone pulling by imaging the deformation of collagen fibers using DIC microscopy. Whereas collagen fibers were displaced upon fibroblast contact, neurites grew without displacing adjacent collagen fibers (Figure S2A; Video S4). To infer actual forces imposed by the growth cones, we developed a 3D traction force reconstruction algorithm that uses fiber displacement data retrieved by 3D reflection microscopy imaging together with rheometrical matrix stiffness analysis (Broguiere et al., 2018; Legant et al., 2010) (Figures 4C–4E, S2B, and S2C; Video S5). While fibroblasts pulled with an average force of 17 ± 4 Pa, reaching peaks of 60 Pa, we found that neurons, by contrast, exerted only minimal pulling forces that were at least 20 times weaker than those by fibroblasts and

CellPress
OPEN ACCESS

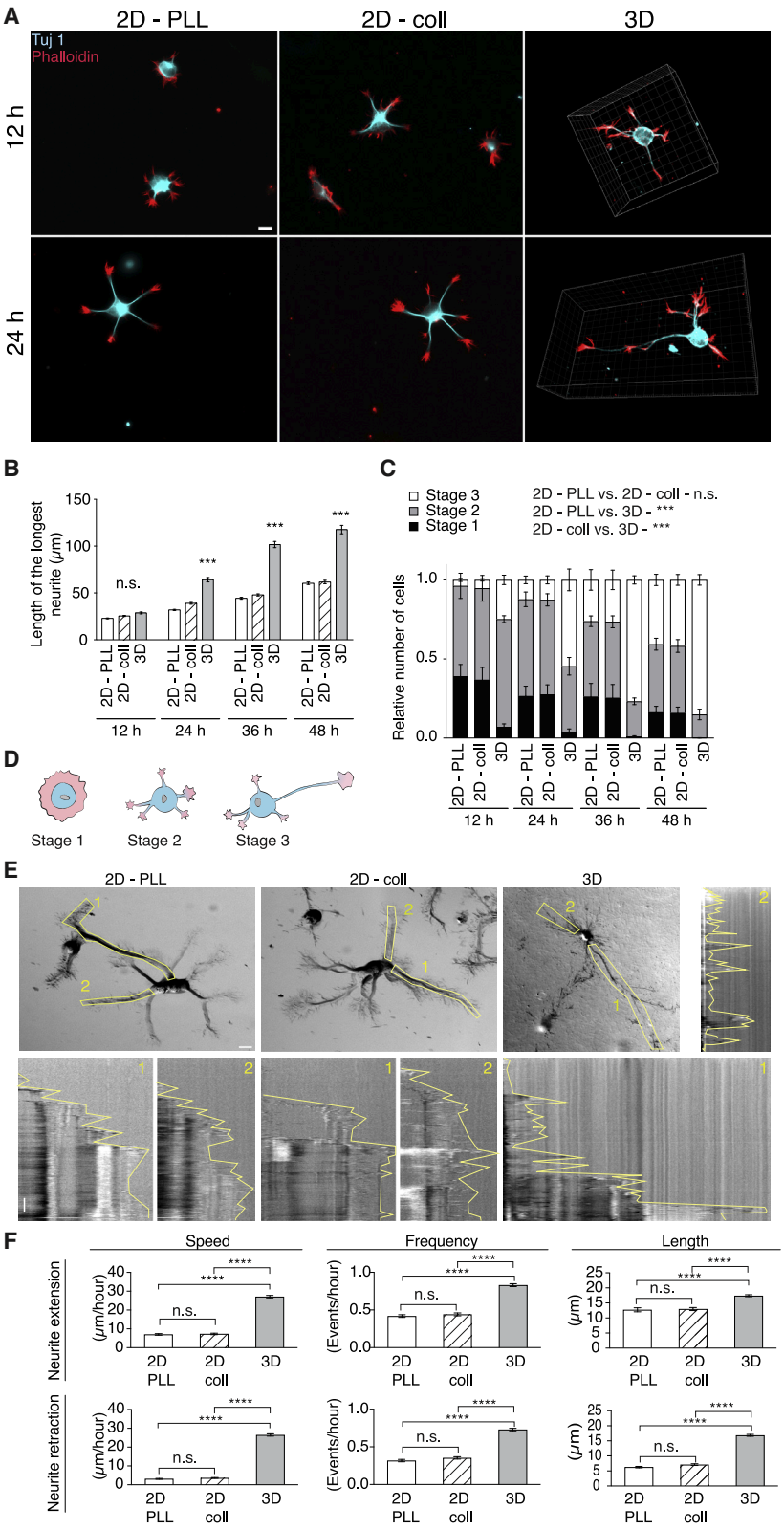

Figure 1. Neurons in 3D Collagen Display Longer Neurites and a Distinct Mode of Growth Compared to 2D Substrates

(A) Tuj 1 (cyan) and Phalloidin (red) immunolabeled hippocampal neurons fixed at 12 and 24 h. Scale bar, 10 μm.

(B) Length of the longest neurite of indicated conditions after 12, 24, 36, and 48 h. n = 4 experiments, n ≥ 340 cells. The significance refers to the three conditions at each time point. Values are plotted as means ± SEM. ***p < 0.001; n.s., not significant by one-way ANOVA followed by Tukey's post-test.

(C) Morphological polarity of hippocampal neurons grown in indicated conditions at 12, 24, 36, and 48 h. n = 4, n ≥ 340. ***p < 0.001, n.s., not significant by an ordinal logistic regression model.

(D) Illustration of the polarity stages for the morphological assessment of polarity.

(E) DIC time-lapse minimum intensity projections and kymographs of selected neurites in indicated conditions. Horizontal scale bar, 10 μm. Vertical scale bar, 6 h.

(F) Speed, frequency, and length of extension and retraction events of the DIC time lapse. n = 4, n ≥ 45. Values are plotted as means ± SEM. ****p < 0.0001; n.s., not significant by one-way ANOVA followed by Tukey's post-test.

See also Figure S1 and Videos S1 and S2.

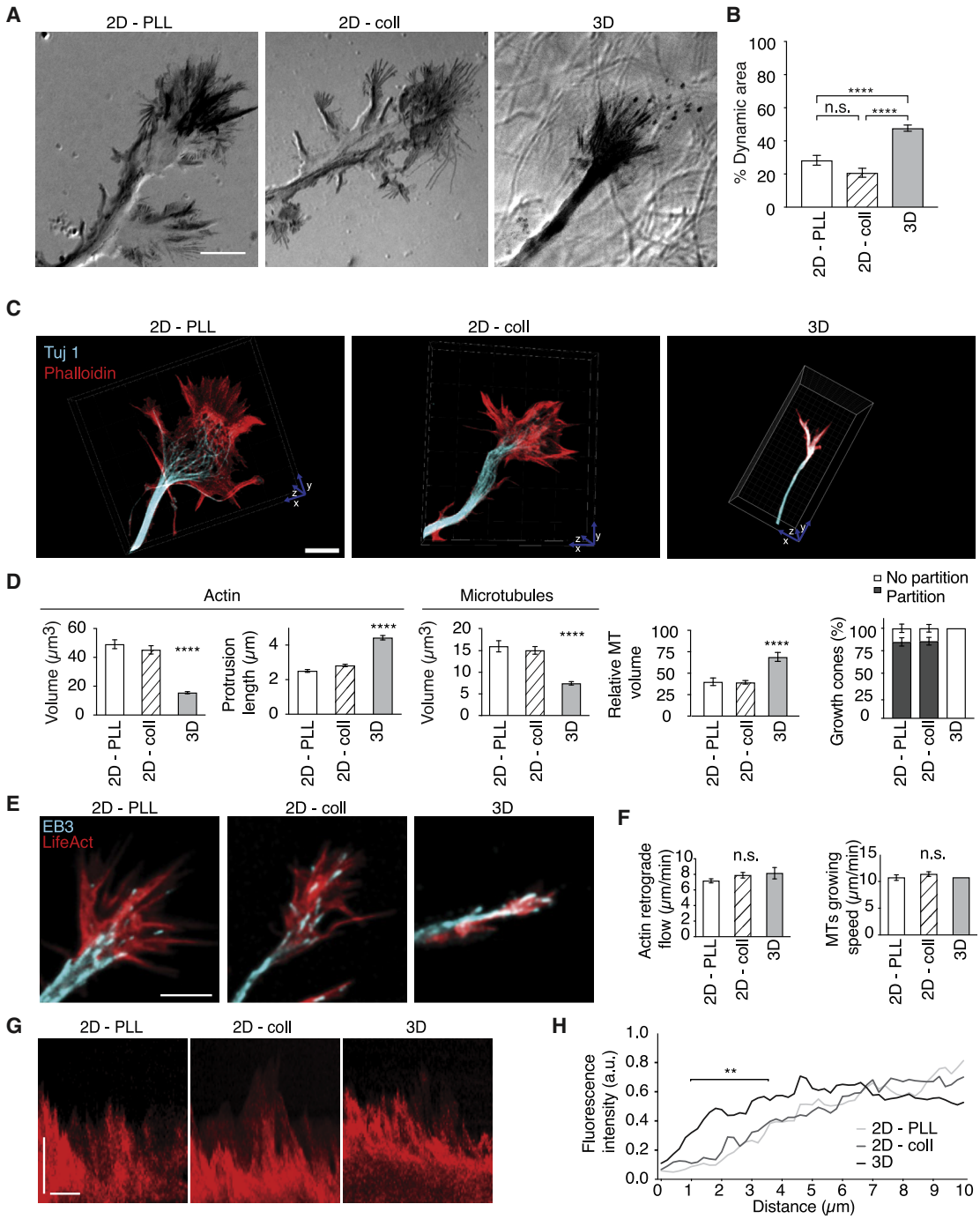

Figure 2. Growth Cone Structure and Dynamics in 3D Differ from 2D Conditions, and Microtubules Protrude Closer to the Leading Edge

(A) DIC time-lapse minimum intensity projections of growth cones in indicated conditions. Scale bar, 5 μm.

(B) Percentage of active area (darker) normalized by the growth cone area. n = 3, n ≥ 35. Values are plotted as means ± SEM. ****p < 0.0001; n.s., not significant by one-way ANOVA followed by Tukey's post-test.

(C) STED images of Tuj 1 (cyan) and phalloidin (red) immunolabeled growth cones. Scale bar, 5 μm.

(D) Volume of actin and microtubules, actin protrusion length and microtubule (MT) actin ratio; calculated from the surface area. Classification of growth cones with and without partition into peripheral and central domains. n = 3, n ≥ 90. Values are plotted as means ± SEM. ****p < 0.0001, by one-way ANOVA followed by Tukey's post-test.

(E) EB3-mNeonGreen (cyan) and Lifeact-RFPruby (red) transfected neurons. Scale bar, 5 μm.

(F) Cytoskeletal dynamics of growth cones in indicated conditions. n = 3, n ≥ 34. Values are plotted as means ± SEM. n.s., not significant by one-way ANOVA followed by Tukey's post-test.

(legend continued on next page)

indistinguishable from measurement noise (Figures 4C–4E; Video S5). Thus, neurons grow axons without exerting measurable pulling forces on their environment.

Axon Growth Is Independent of Adhesions in 3D Matrices

Migratory cells that pull along the substrate engage adhesions to interact with their environments (Bodor et al., 2020). As neurons extended their axons without pulling on the matrix, we asked whether adhesions are necessary for axon growth. We therefore blocked adhesions by using an anti-β1-integrin antibody or chelating divalent cations using ethylenediaminetetraacetic acid (EDTA) (Nikolovski and Mooney, 2000) and assessed axon growth in 3D. As expected, fibroblasts, which served as a positive control for active adhesions, reduced their pulling on the matrix after anti-β1-integrin treatment, and pulling was almost abolished after EDTA treatment (Figures 5A and 5B; Video S6). Time-lapse DIC recordings showed that while fibroblasts changed their migratory mode from exploratory throughout the matrix to almost nonmoving rounded cells after EDTA treatment, neurons grew their axons undisturbed after both treatments. Indeed, the speed, frequency, and length of extension and retraction events remained unchanged (Figures 5C and 5D; Video S6).

To directly test whether CNS neurons could extend axons without adhesions, we embedded neurons in polyethylene glycol (PEG) matrices (Figure 5E; Video S7), which are inert to adhesion formation (Broguiere et al., 2019). Indeed, in PEG matrices, neurons grew in a pattern indistinguishable from neurons grown in collagen (Figures S3C and S3D; Video S7). The number of Tau-1$^+$ axons was comparable in 3D PEG and collagen matrices in culture after 24 h (Figures S3A and S3B), and the average length of the longest neurite was indistinguishable between 3D PEG and collagen matrices (Figure 5F). Thus, embryonic hippocampal neurons can polarize and extend their axon in 3D independently of adhesions.

DISCUSSION

The last decades saw a better understanding of how axons are guided to their targets (Stoeckli, 2018). Still, relatively little is known about how axons actually grow. In this study, we show that developing CNS neurons extend axons without pulling on the matrix and without the need for adhesions in 3D. The growth of axons in 3D matrices is faster, more dynamic, and more physiological than on comparable 2D substrates. Our findings highlight that adhesions are dispensable for axon growth and that developing hippocampal neurons grow in an amoeboid mode.

The Physiological Relevance of Axon Growth in a 3D Matrix

During early development, axons grow in a complex, highly dynamic environment composed of progenitor cells, differentiating cells, and an extracellular space filled with matrix molecules, guidance cues, and pioneering axon tracts (Chen et al., 2017; Franze et al., 2013). Such a complex environment makes it difficult to decipher the cell-intrinsic mechanisms underlying axon growth. Traditional neuronal cell culture experiments provide the advantage of being able to study axon growth properties in a defined environment. This environment, however, is typically represented by a flat surface of glass or plastic, neglecting the stiffness, dimensionality, confinement, or structure of embryonic CNS tissue (Kaech and Banker, 2006).

We show here that neurons grown on 2D surfaces have a distinct growth pattern compared to neurons grown in 3D matrices or slice culture. In 3D HA, PEG and collagen matrices neurons polarize and resemble the physiological growth observed in slice culture. Despite different biophysical properties among these matrices, including porosity, structure, and fiber size, physiological axon growth is not compromised. However, what these matrices have in common is their stiffness and dimensionality, which resemble *in vivo* characteristics (Broguiere et al., 2019; Iwashita et al., 2014).

Taken together, the 3D collagen matrix is an effective model to use a reductionist approach in investigating cell biology questions in neurons. It models the complex environment found *in vivo* but enables manipulations of specific biophysical properties to investigate their roles in the physiological polarization of neurons. Our study thereby lays the foundation to study the cytoskeletal mechanisms underlying axon growth in the complex environment of the developing brain.

Adhesions Are Dispensable for Axon Growth in 3D

Adhesions are essential for synapse formation and neuronal plasticity; they perceive guidance cues for growing axons and facilitate axon stability (Myers et al., 2011). Despite the prevailing view (for decades) that neurons need adhesions to extend axons by fixing the growth cone to the matrix, using actomyosin-mediated pulling to move the growth cone and the trailing axon forward (Mitchison and Kirschner, 1988), earlier reports were inconsistent with this finding. It was described that at least under special conditions, neurons are able to extend an axon in a liquid medium (Letourneau et al., 1987). Models for axon growth have been based on various types of neurons, including cultured dorsal root ganglia (DRG) and *Aplysia* bag cell neurons (Miller and Suter, 2018). In fact, there could be differences in adhesive influence on axon growth between central and peripheral neurons (Betz et al., 2011; Koch et al., 2012; Nichol et al., 2019). We therefore directly tested the role of adhesions by growing CNS neurons in 3D matrices. Indeed, by blocking adhesions in two different ways and growing hippocampal neurons in PEG matrices, which are inert to adhesion formation, we found adhesion sites are dispensable for axon outgrowth.

This sheds new light on two apparent paradoxical deductions in axonal outgrowth. First, formerly postulated pulling mechanisms would cause matrix deformation in the soft CNS (Betz

(G) Kymographs from live-cell imaging of growth cones transfected with Lifeact-RFPruby. Horizontal scale bar, 1 min. Vertical scale bar, 10 μm.
(H) EB3 fluorescence intensity relative to the leading edge of the growth cone. N = 3, n ≥ 35. Values are plotted as means ± SEM. **p < 0.01, by one-way ANOVA followed by Tukey's post-test.
See also Video S3.

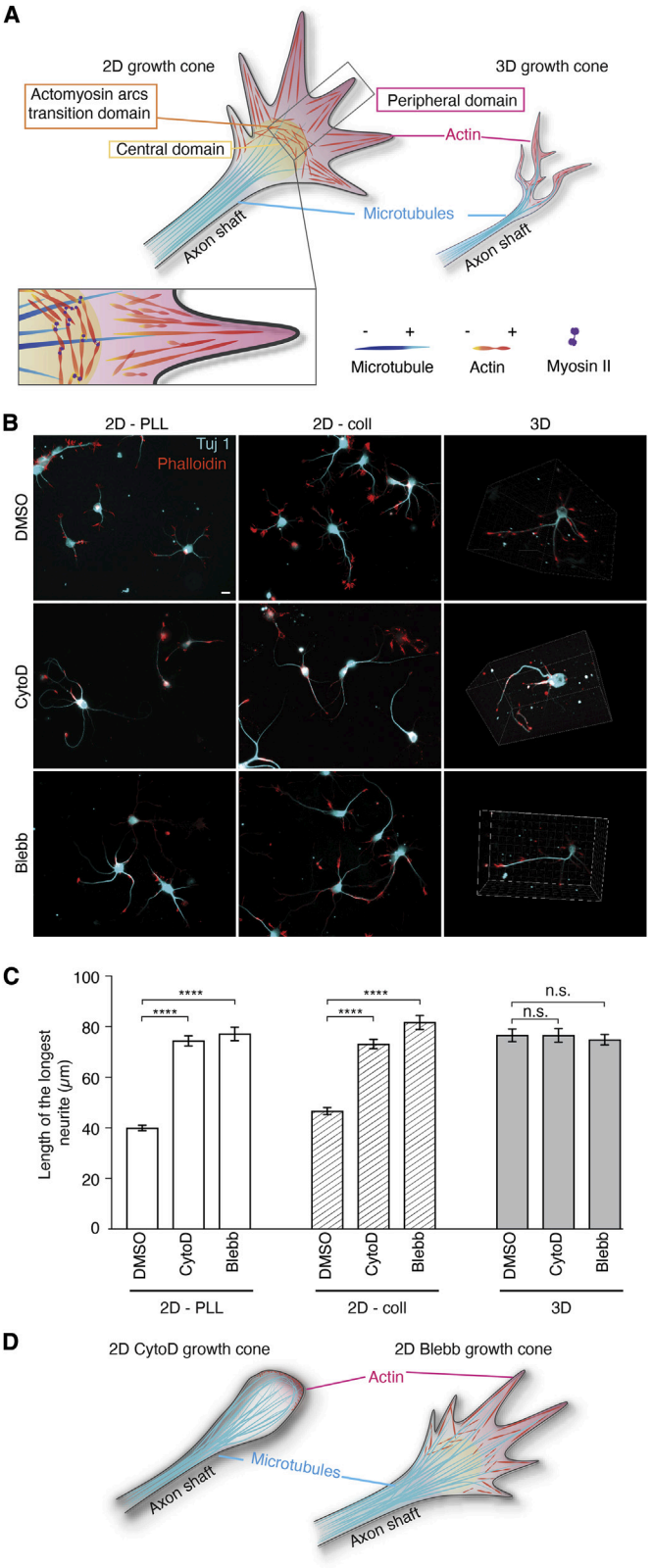

Figure 3. Actin Depolymerization or Relaxation of Actomyosin Arcs Does Not Increase Axonal Growth in 3D

(A) Scheme of growth cones in 2D and 3D.

(B) Tuj 1 (cyan) and phalloidin (red) immunolabeled neurons treated with DMSO, cytochalasin D (CytoD), or blebbistatin (Blebb). Scale bar, 10 μm.

(C) Length of the longest neurite after 24 h of DMSO, CytoD, or Blebb treatments. n = 3, n ≥ 191. Values are plotted as means ± SEM. ****p < 0.0001; n.s., not significant by one-way ANOVA followed by Tukey's post-test.

(D) Scheme of growth cones in 2D after CytoD or Blebb treatment.

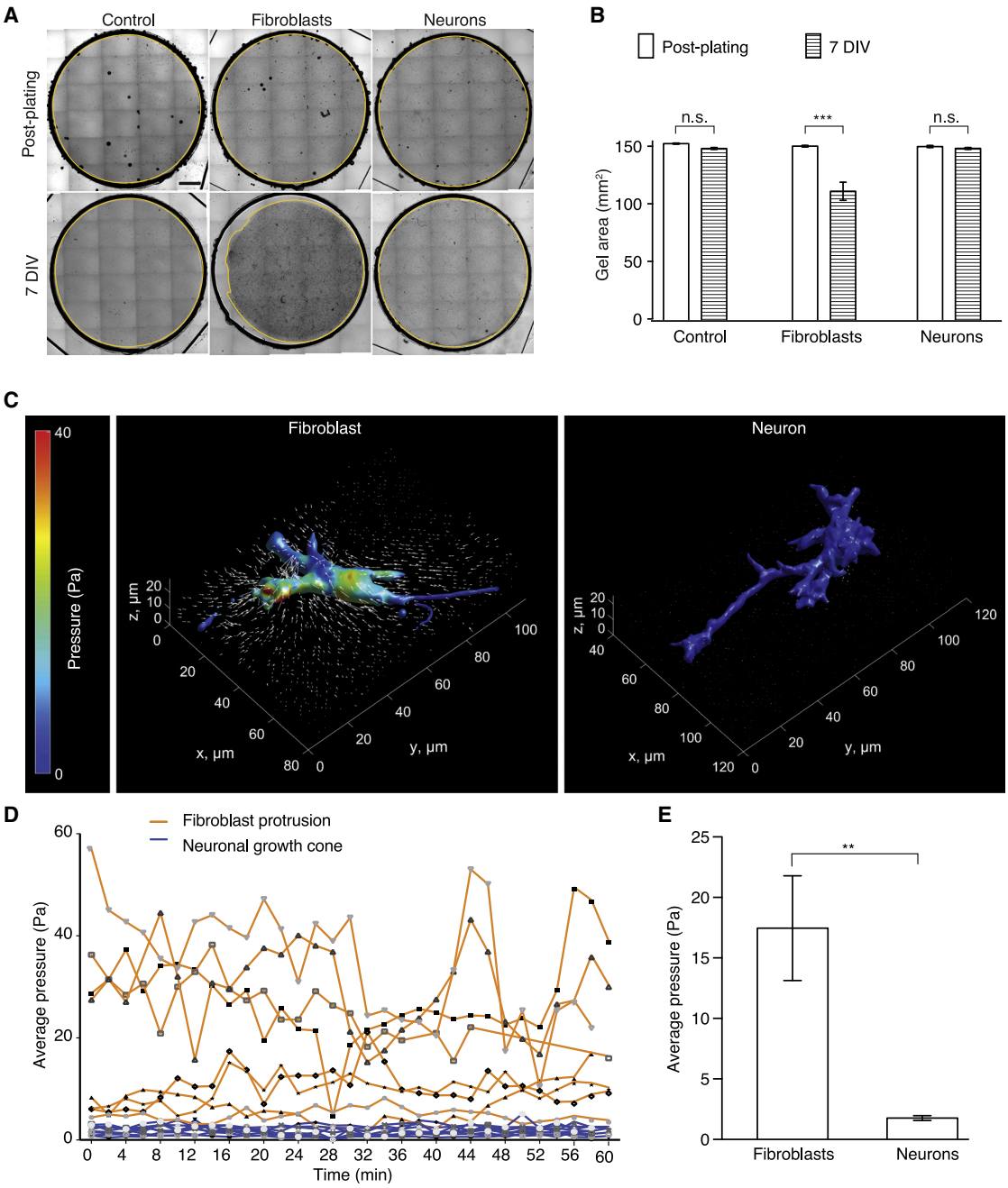

Figure 4. Growth Cone Motility in 3D Is Amoeboid

(A) Matrix contraction assay. Stitched tilescans of gels without cells (control), with meningeal fibroblasts or neurons after plating and after 7 days. Scale bar, 2 mm.

(B) Size of gel area upon plating and after 7 days. n = 3, n = 11. Values plotted as means ± SEM. ***p < 0.001; n.s., not significant by one-way ANOVA followed by Tukey's post-test.

(C) 3D view of stress applied by the cells and displacement of the matrix (white arrows, amplified 10-fold) after analysis of traction force microscopy.

(D) Average pressure exerted by single fibroblast processes or axonal growth cones, as measured by traction force microscopy over time. Each line represents one cell.

(E) Average stress values from n = 8 experiments, n = 9 cells × 30 time points. Statistics by Student's t test. Values are plotted as means ± SEM. **p < 0.01. See also Figure S2 and Videos S4 and S5.

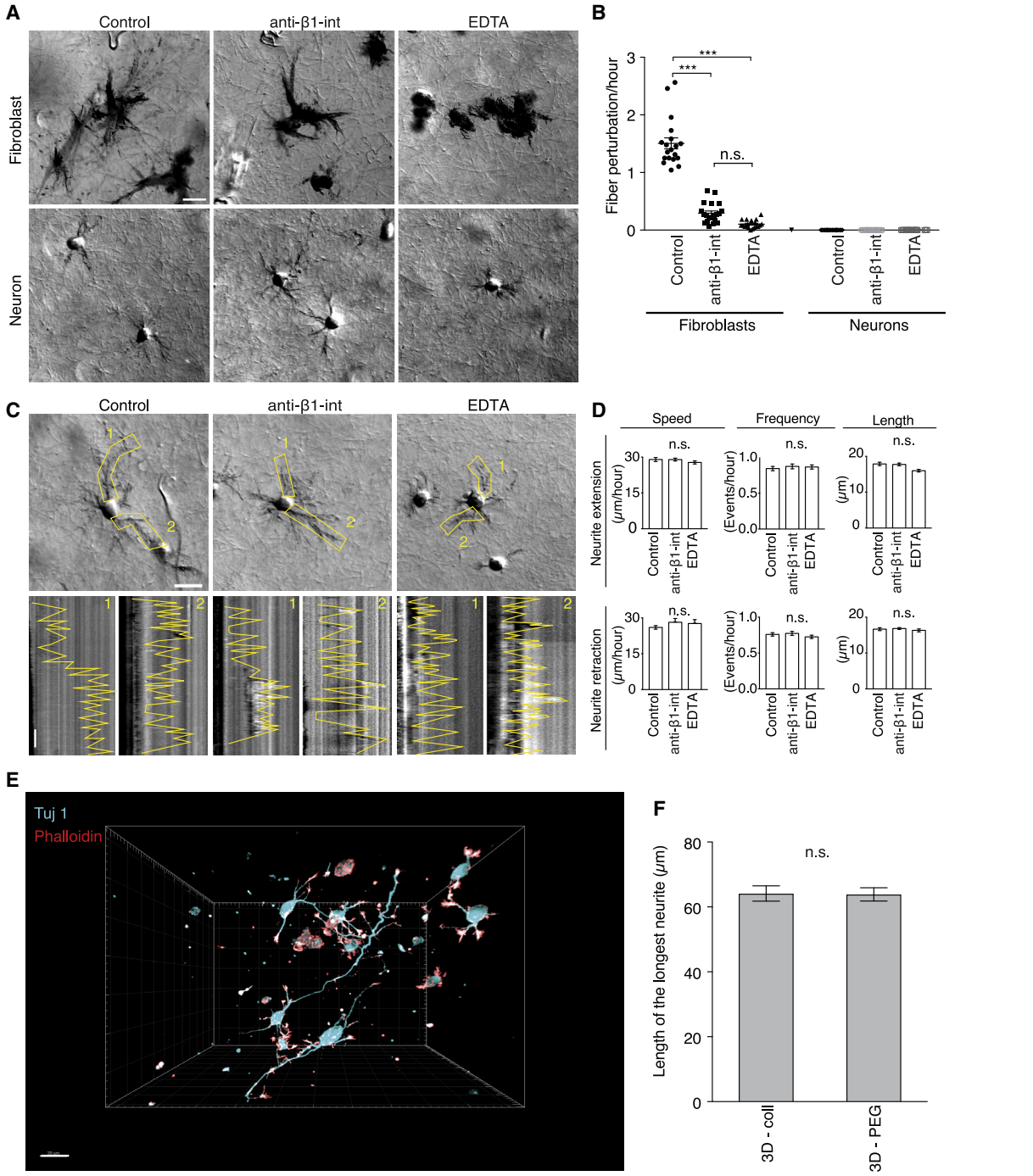

Figure 5. Axon Growth in 3D Is Independent of Adhesions

(A) DIC time-lapse minimum intensity projection of fibroblasts and neurons under indicated conditions. Scale bar, 20 μm.

(B) Fiber perturbation frequency of fibroblasts and neurons under indicated conditions. n = 3, n = 12. Values are plotted as means ± SEM. ***$p < 0.001$; n.s., not significant by one-way ANOVA followed by Tukey's post-test.

(C) DIC time-lapse minimum intensity projections and kymographs of selected neurites control, anti-β1-integrin antibody, and EDTA treated neurons. Scale bar, 10 μm.

(D) Speed, frequency, and length of extension and retraction events in the time lapse. n = 3, n ≥ 31. Values are plotted as means ± SEM. n.s., not significant by one-way ANOVA followed by Tukey's post-test.

(E) Tuj 1 (cyan) and phalloidin (red) immunolabeled neurons in a 3D PEG gel. Scale bar, 50 μm.

(legend continued on next page)

et al., 2011; Bray, 1984). This is rectified by our findings that CNS axons grow without pulling. Second, degradation of extracellular matrix by metalloproteinases (Santiago-Medina et al., 2015) would make it difficult for axons to form adhesion points in the growth cone vicinity. The demonstrated growth of axons, independent of adhesions and pulling, instead could function undisturbed upon extracellular matrix digestion. This suggests that while adhesion sites could be important for haptic guidance signals, where traction forces can be generated (Dominici et al., 2017; Moore et al., 2009, 2012), as well as for fixing the axon shaft, morphogenetic changes are rather driven by neuron-intrinsic forces, which require less interaction with the CNS environment and are independent of pulling.

The Role of Actin Arcs during Axon Extension in 3D

Exploring the growth behavior of embryonic hippocampal neurons, we found that they grow longer axons and polarize faster in 3D collagen compared to 2D conditions. Detailed super-resolution analysis showed that the growth cone is smaller in 3D conditions than in 2D conditions, reminiscent of fast-growing growth cones *in vivo* (Ertürk et al., 2007; Harris et al., 1987; Knobel et al., 1999). Importantly, the growth cone in 3D was devoid of actin arcs such that microtubules can protrude further to the leading edge and thereby accelerate axon growth and neuronal polarization (Hellal et al., 2011; Ruschel et al., 2015; Witte et al., 2008). On the contrary, in 2D cultures, actin arcs restrict microtubules from protruding to the leading edge and inhibit growth (Dupraz et al., 2019; Schaefer et al., 2002). This is the consequence of growth cone architecture in 2D, where microtubules coupled to actin arcs move centripetally to the central domain (Lowery and Van Vactor, 2009; Schaefer et al., 2002). Relaxation of actomyosin arcs in the growth cone leads to enhanced protrusion of microtubules toward the leading edge (Bradke and Dotti, 1999; Dupraz et al., 2019).

We propose that relatively stiff unphysiological 2D conditions might augment actin arc formation in CNS neurons. Consistent with this view, migrating human sarcoma cells form arcs on 64-kPa stiff substrates. On soft substrates with a stiffness of 0.5 kPa, comparable to the stiffness of ~0.2 kPa of our collagen matrix or the developing mouse CNS (Iwashita et al., 2014), just a small percentage of cells formed arcs (Tojkander et al., 2015). Together with other evidence from our lab (Dupraz et al., 2019), we further anticipate that actin arcs might be induced by inhibitory guidance signals and act as a brake allowing the growth cone to steer the axon effectively through its developing environment. Thus, actin arcs might not be an essential component for axon growth; rather, they act negatively on growth downstream of inhibitory guidance cues (Dupraz et al., 2019; Miller and Suter, 2018).

CNS Axons Grow in an Amoeboid Mode

The growth cone can be seen as a separate migratory unit of the neuron that navigates through the environment to its appropriate target like a "leucocyte on a leash" (Miller and Suter, 2018; Pfenninger, 1986). Thus, the cellular physiology of axon growth might be comparable to cell migration. We demonstrate that in 3D collagen gels, neurons do not contract the matrix unlike fibroblasts. Therefore, growth cones may not use a mesenchymal mode of migration, as used by fibroblasts, to pull themselves forward through their adhesions (Even-Ram and Yamada, 2005), but rather an amoeboid type of movement characterized by engaging lower adhesive force for their migration (Lämmermann and Sixt, 2009).

Different modes of amoeboid migration have been described previously (Lämmermann and Sixt, 2009). Amoeboid cells either migrate by protruding their leading front as an actin-free membrane bleb that is inflated by actomyosin-driven contractile forces or protrusions that are polymerization driven (Lämmermann et al., 2008). The latter form of amoeboid migration is independent of adhesions and actomyosin contraction mediated forces. The balance between these forces describes which type of amoeboid movement the cell is using. In accordance, we can classify the growth cone as a protrusive migratory element where adhesive forces are low or even neglectable. We can also neglect blebbing by myosin II-dependent contraction, since hippocampal neurons grew undisturbed in 3D upon blebbistatin treatment. In fact, we did not observe any blebbing events as found in other cells (Bodor et al., 2020; Charras and Paluch, 2008). This kind of amoeboid-migration mode has been observed in dendritic cells and neutrophils (Lämmermann et al., 2008). Microtubules are necessary for axon elongation, as depolymerizing microtubules abolishes axon growth (Dupraz et al., 2019; Neukirchen and Bradke, 2011; Witte et al., 2008), whereas moderate pharmacological or molecular stabilization of microtubules, which causes microtubule growth, elicits axon growth (Ertürk et al., 2007; Gomis-Rüth et al., 2008; Witte et al., 2008). We therefore propose an amoeboid type of migration, which is driven by microtubule polymerization and independent of actin.

Other cell types, including leucocytes and several tumor cell lines, are known to change their mode of migration depending on environmental conditions (Lämmermann and Sixt, 2009; Malawista et al., 2000; Poincloux et al., 2011; Sroka et al., 2002; Wolf et al., 2003). It will be important to determine whether neurons are also able to transform to different modes of growth.

Conclusions

Our findings show that embryonic CNS neurons grow in an amoeboid mode without the need for adhesions. Together with the perspective that lesioned axons can regenerate by reactivating their developmental growth program (Hilton and Bradke, 2017), this implies that regeneration of adult CNS axons might be facilitated by an amoeboid mode of growth rather than the actomyosin contractive mesenchymal migration mode. Approaches such as enhancing microtubule protrusion in the injured axon (Hellal et al., 2011; Ruschel et al., 2015) may be one method to achieve this. Thus, a better understanding of

(F) Length of the longest neurite after 24 h in collagen and PEG gels. n = 3, n > 382. Statistics by Student's t test. Values are plotted as means ± SEM. n.s., not significant.
See also Figure S3 and Videos S6 and S7.

the cytomechanics underlying axon growth will help to tune the growth apparatus to elicit axon regeneration.

STAR★METHODS

Detailed methods are provided in the online version of this paper and include the following:

- KEY RESOURCES TABLE
- RESOURCE AVAILABILITY
  - Lead Contact
  - Materials Availability
  - Data and Code Availability
- EXPERIMENTAL MODEL AND SUBJECT DETAILS
  - Animals
  - Primary Cell Culture
- METHOD DETAILS
  - Cell Culture
  - Collagen 3D Matrices
  - Hyaluronic Acid Matrices
  - PEG Gels
  - Contraction Assays
  - Transfections
  - Immunocytochemistry
  - Drug Treatments
  - In Utero Electroporation and Slice Culture
  - Plasmids
  - Imaging Fixed Neurons
  - Contraction Assays
  - DIC Videos
  - STED Imaging
  - Cytoskeleton Dynamics
  - Slice Imaging
  - Reflection/Confocal Traction Force Microscopy
  - Figures
- QUANTIFICATION AND STATISTICAL ANALYSIS
  - Length of the Longest Neurite
  - Branching
  - Polarity Stages and Tau-1 Positive Cells
  - Long-term Videos of Growth Dynamics
  - Growth Cone Morphology by STED Imaging
  - Growth Cone Active Area in DIC Imaging
  - Cytoskeletal Dynamics
  - Fiber Perturbation Frequency
  - Rheometry
  - Traction Force Microscopy Measurements
  - Statistics

SUPPLEMENTAL INFORMATION

Supplemental Information can be found online at https://doi.org/10.1016/j.celrep.2020.107907.

ACKNOWLEDGMENTS

We thank T. Pietralla, T. Stuerner, M. Curcio, A. Correia, A. Husch, S. Stern, B. Hilton, S. Dupraz, M. Pinger, R. Wedlich-Söldner, M. Sixt, K. Kawabata, E. Burnside, and T. Lin for reading and discussing the manuscript. We are thankful to S. Dupraz for providing plasmids. We acknowledge the assistance of M. Schölling from the Image and Data Analysis Facility of the DZNE Bonn for the statistical analysis. T.S. was supported by a Boehringer Ingelheim Fonds, Germany PhD fellowship. This work was further supported by the International Foundation for Research in Paraplegia, Switzerland, Wings for Life, Deutsche Forschungsgemeinschaft (DFG), ERANET AXON REPAIR 01EW1702, and ERANET RATER SCI 01EW1704 (F.B.). F.B. is a member of the excellence cluster ImmunoSensation2 and the SFBs 1089 and 1158 and is a recipient of the Roger de Spoelberch Prize.

AUTHOR CONTRIBUTIONS

T.E.S. and F.B. conceived the project; T.E.S. and F.B. designed research; T.E.S., L.M., and N.B. performed research; T.E.S., B.S., and N.B. analyzed the data; F.B. supervised the research; T.E.S., B.S., and F.B. wrote the paper. T.E.S., B.S., N.B., L.M., M.Z.-W., and F.B. provided feedback and contributed to editing the manuscript.

DECLARATION OF INTERESTS

H. Witte, A. Ertürk, F. Hellal, and F.B. filed a patent on the use of microtubule-stabilizing compounds for the treatment of lesions of CNS axons (European patent number 1858498; European patent application EP 11 00 9155.0; U.S. patent application 11/908,118).

Received: March 27, 2020
Revised: May 26, 2020
Accepted: June 23, 2020
Published: July 21, 2020

REFERENCES

Benoit, M., Gabriel, D., Gerisch, G., and Gaub, H.E. (2000). Discrete interactions in cell adhesion measured by single-molecule force spectroscopy. Nat. Cell Biol. *2*, 313–317.

Betz, T., Koch, D., Lu, Y.-B., Franze, K., and Käs, J.A. (2011). Growth cones as soft and weak force generators. Proc. Natl. Acad. Sci. USA *108*, 13420–13425.

Blanquie, O., and Bradke, F. (2018). Cytoskeleton dynamics in axon regeneration. Curr. Opin. Neurobiol. *51*, 60–69.

Bodor, D.L., Pönisch, W., Endres, R.G., and Paluch, E.K. (2020). Of cell shapes and motion: the physical basis of animal cell migration. Dev. Cell *52*, 550–562.

Bradke, F., and Dotti, C.G. (1997). Neuronal polarity: vectorial cytoplasmic flow precedes axon formation. Neuron *19*, 1175–1186.

Bradke, F., and Dotti, C.G. (1999). The role of local actin instability in axon formation. Science *283*, 1931–1934.

Bray, D. (1984). Axonal growth in response to experimentally applied mechanical tension. Dev. Biol. *102*, 379–389.

Broguiere, N., Isenmann, L., and Zenobi-Wong, M. (2016). Novel enzymatically cross-linked hyaluronan hydrogels support the formation of 3D neuronal networks. Biomaterials *99*, 47–55.

Broguiere, N., Isenmann, L., Hirt, C., Ringel, T., Placzek, S., Cavalli, E., Ringnalda, F., Villiger, L., Züllig, R., Lehmann, R., et al. (2018). Growth of epithelial organoids in a defined hydrogel. Adv. Mater. *30*, e1801621.

Broguiere, N., Husch, A., Palazzolo, G., Bradke, F., Madduri, S., and Zenobi-Wong, M. (2019). Macroporous hydrogels derived from aqueous dynamic phase separation. Biomaterials *200*, 56–65.

Charras, G., and Paluch, E. (2008). Blebs lead the way: how to migrate without lamellipodia. Nat. Rev. Mol. Cell Biol. *9*, 730–736.

Chen, V.S., Morrison, J.P., Southwell, M.F., Foley, J.F., Bolon, B., and Elmore, S.A. (2017). Histology atlas of the developing prenatal and postnatal mouse central nervous system, with emphasis on prenatal days E7.5 to E18.5. Toxicol. Pathol. *45*, 705–744.

Dominici, C., Moreno-Bravo, J.A., Puiggros, S.R., Rappeneau, Q., Rama, N., Vieugue, P., Bernet, A., Mehlen, P., and Chédotal, A. (2017). Floor-plate-

derived netrin-1 is dispensable for commissural axon guidance. Nature *545*, 350–354.

Dupraz, S., Hilton, B.J., Husch, A., Santos, T.E., Coles, C.H., Stern, S., Brakebusch, C., and Bradke, F. (2019). RhoA controls axon extension independent of specification in the developing brain. Curr. Biol. *29*, 3874–3886.e9.

Elsdale, T., and Bard, J. (1972). Collagen substrata for studies on cell behavior. J. Cell Biol. *54*, 626–637.

Ertürk, A., Hellal, F., Enes, J., and Bradke, F. (2007). Disorganized microtubules underlie the formation of retraction bulbs and the failure of axonal regeneration. J. Neurosci. *27*, 9169–9180.

Even-Ram, S., and Yamada, K.M. (2005). Cell migration in 3D matrix. Curr. Opin. Cell Biol. *17*, 524–532.

Flynn, K.C., Hellal, F., Neukirchen, D., Jacob, S., Tahirovic, S., Dupraz, S., Stern, S., Garvalov, B.K., Gurniak, C., Shaw, A.E., et al. (2012). ADF/cofilin-mediated actin retrograde flow directs neurite formation in the developing brain. Neuron *76*, 1091–1107.

Forscher, P., and Smith, S.J. (1988). Actions of cytochalasins on the organization of actin filaments and microtubules in a neuronal growth cone. J. Cell Biol. *107*, 1505–1516.

Franze, K., Janmey, P.A., and Guck, J. (2013). Mechanics in neuronal development and repair. Annu. Rev. Biomed. Eng. *15*, 227–251.

Garvalov, B.K., Flynn, K.C., Neukirchen, D., Meyn, L., Teusch, N., Wu, X., Brakebusch, C., Bamburg, J.R., and Bradke, F. (2007). Cdc42 regulates cofilin during the establishment of neuronal polarity. J. Neurosci. *27*, 13117–13129.

Gomez, T.M., and Letourneau, P.C. (2014). Actin dynamics in growth cone motility and navigation. J. Neurochem. *129*, 221–234.

Gomis-Rüth, S., Wierenga, C.J., and Bradke, F. (2008). Plasticity of polarization: changing dendrites into axons in neurons integrated in neuronal circuits. Curr. Biol. *18*, 992–1000.

Grinnell, F., and Petroll, W.M. (2010). Cell motility and mechanics in three-dimensional collagen matrices. Annu. Rev. Cell Dev. Biol. *26*, 335–361.

Harris, W.A., Holt, C.E., and Bonhoeffer, F. (1987). Retinal axons with and without their somata, growing to and arborizing in the tectum of Xenopus embryos: a time-lapse video study of single fibres in vivo. Development *101*, 123–133.

Hellal, F., Hurtado, A., Ruschel, J., Flynn, K.C., Laskowski, C.J., Umlauf, M., Kapitein, L.C., Strikis, D., Lemmon, V., Bixby, J., et al. (2011). Microtubule stabilization reduces scarring and causes axon regeneration after spinal cord injury. Science *331*, 928–931.

Hilton, B.J., and Bradke, F. (2017). Can injured adult CNS axons regenerate by recapitulating development? Development *144*, 3417–3429.

Hothorn, T., Bretz, F., and Westfall, P. (2008). Simultaneous inference in general parametric models. Biom. J. *50*, 346–363.

Iwashita, M., Kataoka, N., Toida, K., and Kosodo, Y. (2014). Systematic profiling of spatiotemporal tissue and cellular stiffness in the developing brain. Development *141*, 3793–3798.

Jay, D.G. (2000). The clutch hypothesis revisited: ascribing the roles of actin-associated proteins in filopodial protrusion in the nerve growth cone. J. Neurobiol. *44*, 114–125.

Kaech, S., and Banker, G. (2006). Culturing hippocampal neurons. Nat. Protoc. *1*, 2406–2415.

Knobel, K.M., Jorgensen, E.M., and Bastiani, M.J. (1999). Growth cones stall and collapse during axon outgrowth in Caenorhabditis elegans. Development *126*, 4489–4498.

Koch, D., Rosoff, W.J., Jiang, J., Geller, H.M., and Urbach, J.S. (2012). Strength in the periphery: growth cone biomechanics and substrate rigidity response in peripheral and central nervous system neurons. Biophys. J. *102*, 452–460.

Kunda, P., Paglini, G., Quiroga, S., Kosik, K., and Cáceres, A. (2001). Evidence for the involvement of Tiam1 in axon formation. J. Neurosci. *21*, 2361–2372.

Lämmermann, T., and Sixt, M. (2009). Mechanical modes of 'amoeboid' cell migration. Curr. Opin. Cell Biol. *21*, 636–644.

Lämmermann, T., Bader, B.L., Monkley, S.J., Worbs, T., Wedlich-Söldner, R., Hirsch, K., Keller, M., Förster, R., Critchley, D.R., Fässler, R., and Sixt, M. (2008). Rapid leukocyte migration by integrin-independent flowing and squeezing. Nature *453*, 51–55.

Legant, W.R., Miller, J.S., Blakely, B.L., Cohen, D.M., Genin, G.M., and Chen, C.S. (2010). Measurement of mechanical tractions exerted by cells in three-dimensional matrices. Nat. Methods *7*, 969–971.

Letourneau, P.C., Shattuck, T.A., and Ressler, A.H. (1987). "Pull" and "push" in neurite elongation: observations on the effects of different concentrations of cytochalasin B and taxol. Cell Motil. Cytoskeleton *8*, 193–209.

Lin, C.H., Thompson, C.A., and Forscher, P. (1994). Cytoskeletal reorganization underlying growth cone motility. Curr. Opin. Neurobiol. *4*, 640–647.

Lowery, L.A., and Van Vactor, D. (2009). The trip of the tip: understanding the growth cone machinery. Nat. Rev. Mol. Cell Biol. *10*, 332–343.

Malawista, S.E., de Boisfleury Chevance, A., and Boxer, L.A. (2000). Random locomotion and chemotaxis of human blood polymorphonuclear leukocytes from a patient with leukocyte adhesion deficiency-1: normal displacement in close quarters via chimneying. Cell Motil. Cytoskeleton *46*, 183–189.

Matsuda, T., and Cepko, C.L. (2007). Controlled expression of transgenes introduced by *in vivo* electroporation. Proc. Natl. Acad. Sci. USA *104*, 1027–1032.

Meijering, E., Jacob, M., Sarria, J.-C.F., Steiner, P., Hirling, H., and Unser, M. (2004). Design and validation of a tool for neurite tracing and analysis in fluorescence microscopy images. Cytometry A *58*, 167–176.

Miller, K.E., and Suter, D.M. (2018). An integrated cytoskeletal model of neurite outgrowth. Front. Cell. Neurosci. *12*, 447.

Mitchison, T., and Kirschner, M. (1988). Cytoskeletal dynamics and nerve growth. Neuron *1*, 761–772.

Moore, S.W., Biais, N., and Sheetz, M.P. (2009). Traction on immobilized netrin-1 is sufficient to reorient axons. Science *325*, 166, 166.

Moore, S.W., Zhang, X., Lynch, C.D., and Sheetz, M.P. (2012). Netrin-1 attracts axons through FAK-dependent mechanotransduction. J. Neurosci. *32*, 11574–11585.

Mutterer, J., and Zinck, E. (2013). Quick-and-clean article figures with FigureJ. J. Microsc. *252*, 89–91.

Myers, J.P., Santiago-Medina, M., and Gomez, T.M. (2011). Regulation of axonal outgrowth and pathfinding by integrin-ECM interactions. Dev. Neurobiol. *71*, 901–923.

Neukirchen, D., and Bradke, F. (2011). Cytoplasmic linker proteins regulate neuronal polarization through microtubule and growth cone dynamics. J. Neurosci. *31*, 1528–1538.

Nichol, R.H., 4th, Catlett, T.S., Onesto, M.M., Hollender, D., and Gómez, T.M. (2019). Environmental elasticity regulates cell-type specific RHOA signaling and neuritogenesis of human neurons. Stem Cell Reports *13*, 1006–1021.

Nikolovski, J., and Mooney, D.J. (2000). Smooth muscle cell adhesion to tissue engineering scaffolds. Biomaterials *21*, 2025–2032.

Pfenninger, K.H. (1986). Of nerve growth cones, leukocytes and memory: second messenger systems and growth-regulated proteins. Trends Neurosci. *9*, 562–565.

Poincloux, R., Collin, O., Lizárraga, F., Romao, M., Debray, M., Piel, M., and Chavrier, P. (2011). Contractility of the cell rear drives invasion of breast tumor cells in 3D Matrigel. Proc. Natl. Acad. Sci. USA *108*, 1943–1948.

Riedl, J., Flynn, K.C., Raducanu, A., Gärtner, F., Beck, G., Bösl, M., Bradke, F., Massberg, S., Aszodi, A., Sixt, M., and Wedlich-Söldner, R. (2010). Lifeact mice for studying F-actin dynamics. Nat. Methods *7*, 168–169.

Rösner, H., Möller, W., Wassermann, T., Mihatsch, J., and Blum, M. (2007). Attenuation of actinomyosinII contractile activity in growth cones accelerates filopodia-guided and microtubule-based neurite elongation. Brain Res. *1176*, 1–10.

Rueden, C.T., Schindelin, J., Hiner, M.C., DeZonia, B.E., Walter, A.E., Arena, E.T., and Eliceiri, K.W. (2017). ImageJ2: ImageJ for the next generation of scientific image data. BMC Bioinformatics *18*, 529.

Ruoslahti, E. (1996). Brain extracellular matrix. Glycobiology *6*, 489–492.

Ruschel, J., Hellal, F., Flynn, K.C., Dupraz, S., Elliott, D.A., Tedeschi, A., Bates, M., Sliwinski, C., Brook, G., Dobrindt, K., et al. (2015). Axonal regeneration. Systemic administration of epothilone B promotes axon regeneration after spinal cord injury. Science *348*, 347–352.

Saito, T., and Nakatsuji, N. (2001). Efficient gene transfer into the embryonic mouse brain using in vivo electroporation. Dev. Biol. *240*, 237–246.

Santiago-Medina, M., Gregus, K.A., Nichol, R.H., O'Toole, S.M., and Gomez, T.M. (2015). Regulation of ECM degradation and axon guidance by growth cone invadosomes. Development *142*, 486–496.

Schaefer, A.W., Kabir, N., and Forscher, P. (2002). Filopodia and actin arcs guide the assembly and transport of two populations of microtubules with unique dynamic parameters in neuronal growth cones. J. Cell Biol. *158*, 139–152.

Schelski, M., and Bradke, F. (2017). Neuronal polarization: from spatiotemporal signaling to cytoskeletal dynamics. Mol. Cell. Neurosci. *84*, 11–28.

Schindelin, J., Arganda-Carreras, I., Frise, E., Kaynig, V., Longair, M., Pietzsch, T., Preibisch, S., Rueden, C., Saalfeld, S., Schmid, B., et al. (2012). Fiji: an open-source platform for biological-image analysis. Nat. Methods *9*, 676–682.

Short, C.A., Suarez-Zayas, E.A., and Gomez, T.M. (2016). Cell adhesion and invasion mechanisms that guide developing axons. Curr. Opin. Neurobiol. *39*, 77–85.

Smith, C.L. (1994). Cytoskeletal movements and substrate interactions during initiation of neurite outgrowth by sympathetic neurons in vitro. J. Neurosci. *14*, 384–398.

Sroka, J., von Gunten, M., Dunn, G.A., and Keller, H.U. (2002). Phenotype modulation in non-adherent and adherent sublines of Walker carcinosarcoma cells: the role of cell-substratum contacts and microtubules in controlling cell shape, locomotion and cytoskeletal structure. Int. J. Biochem. Cell Biol. *34*, 882–899.

Stoeckli, E.T. (2018). Understanding axon guidance: are we nearly there yet? Development *145*, dev151415.

Stoppini, L., Buchs, P.A., and Muller, D. (1991). A simple method for organotypic cultures of nervous tissue. J. Neurosci. Methods *37*, 173–182.

Tahirovic, S., and Bradke, F. (2009). Neuronal polarity. Cold Spring Harb. Perspect. Biol. *1*, a001644.

Team, R.D.C. (2008). R: A Language and Environment for Statistical Computing (R Foundation for Statistical Computing).

Tojkander, S., Gateva, G., Husain, A., Krishnan, R., and Lappalainen, P. (2015). Generation of contractile actomyosin bundles depends on mechanosensitive actin filament assembly and disassembly. eLife *4*, e06126.

Tomasek, J.J., Haaksma, C.J., Eddy, R.J., and Vaughan, M.B. (1992). Fibroblast contraction occurs on release of tension in attached collagen lattices: dependency on an organized actin cytoskeleton and serum. Anat. Rec. *232*, 359–368.

Venables, W.N., Ripley, B.D., and Venables, W.N. (2002).). Modern Applied Statistics with S, 4th Edition (Springer).

Witte, H., Neukirchen, D., and Bradke, F. (2008). Microtubule stabilization specifies initial neuronal polarization. J. Cell Biol. *180*, 619–632.

Wolf, K., Mazo, I., Leung, H., Engelke, K., von Andrian, U.H., Deryugina, E.I., Strongin, A.Y., Bröcker, E.B., and Friedl, P. (2003). Compensation mechanism in tumor cell migration: mesenchymal-amoeboid transition after blocking of pericellular proteolysis. J. Cell Biol. *160*, 267–277.

STAR★METHODS

KEY RESOURCES TABLE

REAGENT or RESOURCE	SOURCE	IDENTIFIER
Antibodies		
Mouse anti-Tau1 Clone PC1C6	Millipore	Cat#MAB3420; RRID:AB_94855
Rabbit anti-Tubulin β 3 (TUBB3) Antibody	Sigma-Aldrich	Cat#T2200; RRID: AB_262133
Donkey anti-mouse IgG Alexa Fluor 568	Invitrogen	Cat#A10037; RRID: AB_2534013
Donkey anti -rabbit IgG Alexa Fluor 488	Invitrogen	Cat#A21206; RRID: AB_2535792
AlexaFluor 594 anti-Tubulin beta 3 (TUBB3) Antibody	Biolegend	Cat# 801207; RRID: AB_2650635
Mouse Anti-Ingetrin beta 1 Monoclonal Antibody Clone P5D2	Abcam	Cat#ab24693; RRID: AB_448230
Chemicals, Peptides, and Recombinant Proteins		
(-)-Blebbistatin	Sigma	B0560; CAS: 856925-71-8
Cytochalasin D	Enzo Life Sciences	ALX-380-031; CAS: 22144-77-0
Dimethyl sulfoxide (DMSO)	Sigma-Aldrich	D5879
Collagen, Rat tail type I	Merck Millipore	Cat#08-155
Hyaluronic acid sodium salt	Sigma	Cat#53747
FXIIIa 200 U/mL	Fibrogammin, CSL Behring	N/A
4arm-PEG-vinylsulfone	(Broguiere et al., 2019)	N/A
HA-TG	(Broguiere et al., 2016)	N/A
Critical Commercial Assays		
Nucleofector Kits for Mouse Neurons	Lonza	VPG-1001
Experimental Models: Organisms/Strains		
Mouse: Adult C57Bl6/J	Charles River	N/A
Recombinant DNA		
pTub-alpha1-mtGFP	This paper; Addgene	Cat#138981
pTub-alpha1-DsRED	Addgene	Cat#17707
pCMV-Zsgreen-N1	Takara	Cat #632448
pCAG-mGFP	Addgene	Cat#14757
LifeAct-mRFPruby	(Riedl et al., 2010)	N/A
Software and Algorithms		
Imaris v8.2	Bitplane AG	
ImageJ	NIH	RRID: SCR_002074; https://imagej.nih.gov/ij/
Traction Force Microscopy	Broguiere et al., 2016; Broguiere et al., 2019	https://github.com/nbroguiere/TFM
MATLAB 2017	MathWorks Inc, Natick, Massachusetts, USA	N/A
Huygens Professional v17.04	Scientific Volume Imaging	N/A
Imaris 8.2	Bitplane	N/A

RESOURCE AVAILABILITY

Lead Contact

Further information and requests for resources and reagents should be directed to and will be fulfilled by the Lead Contact Frank Bradke (Frank.Bradke@dzne.de). There are no restrictions on any data or materials presented in this paper.

Materials Availability

Plasmids generated in this study have been deposited to Addgene #138981.

Data and Code Availability

The datasets supporting the current study have not been deposited in a public repository. The reported data is archived on file servers at the German Center for Neurodegenerative Diseases (DZNE), and are available from the corresponding author on request. The code for 3D traction force microscopy is available at https://github.com/nbroguiere/TFM.

EXPERIMENTAL MODEL AND SUBJECT DETAILS

Animals

All animal experiments were performed in accordance with the Animal Welfare Act and the guidelines of the North Rhine-Westphalia State Environment Agency (Landesamt für Natur, Umwelt und Verbraucherschutz (LANUV)). The animals were group housed (up to 5 mice per cage) with room temperature controlled at 21–22°C, and an artificial 12 h light:dark cycle (lights off at 6:00 pm). Mice were given food and water *ad libitum* throughout the experiment.

Primary Cell Culture

Primary mouse hippocampal cell culture was done from E16.5-17.5 embryos of both genders of C57BL/6J mice. Cells were grown at 36.5°C and 5% CO_2.

METHOD DETAILS

Cell Culture

Primary mouse (C57BL/6J) hippocampal neurons were dissected from E16.5–E17.5 brains and cultured as described (Garvalov et al., 2007). The hippocampal region of the cortex was dissected, trypsinized and cultured for 1 to 2 days. Cells were plated on poly-L-lysine (PLL) (Sigma), or PLL and then collagen type I (from rat tail, Merck Millipore, 100 μg/mL), coated glass coverslips, in 3 cm culture dishes, with minimum essential medium (MEM) (GIBCO) and 10% horse serum (HS) (GIBCO). After 2 h, the medium was changed to N2 [1% Neuropan2 (PanBiotech), 1 mM Sodium pyruvate (Sigma), 0.6% Glucose (Merck), 0.22% Sodium bicarbonate (Sigma), 2 mM L-Glutamine (GIBCO), 1x MEM].

Collagen 3D Matrices

Neurons or meningeal fibroblasts were encapsulated in a collagen matrix at densities between 0.75 and 1.5 $x10^6$ cells/mL. Collagen at 4.13 mg/mL was mixed with 10x MEM and 5.5% sodium bicarbonate in these proportions: 225 μL collagen, 30 μL 10x MEM and 15 μL 5.5% Sodium bicarbonate (Elsdale and Bard, 1972). Cells in medium were then added at a proportion of 1:3 and gently mixed. The cell-laden hydrogels were plated in glass bottom μ-slides (Ibidi). The gels were let to solidify at 37°C for 20-30 min and then covered with N2 media.

Hyaluronic Acid Matrices

The components for the hyaluronic acid (HA) gels were synthesized as described (Broguiere et al., 2016). Lyophilized aliquots of transglutaminase (TG) cross-linkable HA, functionalized with lysine donor (HA-TG/Lys) and glutamine donor (HA-TG/Gln) peptides, were resuspended at 0.5% (w/v) in saline supplemented with 50 mM TRIS and 50 mM $CaCl_2$, with pH balanced to 7.5 and sterilized by filtration. Then, the two solutions were combined in equal volume, and 3 μL of FXIIIa 200 U/mL (Fibrogammin, CSL Behring) for 80 μL of gel was added, and incorporated quickly by vortexing. Gelation occurred within 1 to 2 min and was left to proceed for 20 min to ensure a stiffness plateau was reached prior to transferring to medium.

PEG Gels

4arm-PEG-vinylsulfone, 20 kDa, was synthesized as described in Broguiere et al. (2019). Lyophilized aliquots were reconstituted as a 20% stock in HEPES 300 mM, pH 7.4. Matrix metalloproteinase (MMP)-cleavable peptides, flanked by two cysteines providing thiols for cross-linking by Michael addition, of sequence Ac-GCRDGPQGIWGQDRCG-NH2 (Bachem), were resuspended at 20 mM in PBS (GIBCO) balanced to pH 6.0. High viscous HA (Sigma 53747) was resuspended in serum-free medium (neurobasal+B27) at 0.5% (w/v). The solutions were then combined in order to have 1.5% PEG content (w/v), stoichiometric thiol:vinylsulfone, and 70% of HA stock as a viscous, non-cross-linkable supplement increasing porosity and avoiding cell sedimentation. The remaining volume was filled with HEPES 300 mM pH 7.4 buffer. Neurons were embedded in the mixture that was set to gel at 37°C for 50 min, and serum-free medium was then added. A media change was performed 1 to 2 h later to wash unreacted components.

Contraction Assays

Neurons or meningeal fibroblasts were incubated one week in a collagen matrix at similar densities to assess the ability of the encapsulated cells to contract the matrix according to the restrained model of contraction (Grinnell and Petroll, 2010). The cells in collagen were placed on a ring delimited imaging chamber of 1.5 cm diameter and images were taken after gelation and after 1 week after detaching the gels from the bottom of the dish.

Transfections

Neurons and fibroblasts were obtained as described above. Cell were transfected using the Nucleofector mouse transfection kit (Lonza) and the following plasmids: pEB3-mNeonGreen, Lifeact-RFPruby, pCAG-mGFP and pTub-alpha1-mGFP. Cells were resuspended in MEM-HS 10% and plated according to the conventional culture methods described above at the higher concentrations of 2 times fold to compensate for transfection-associated loss of viability.

Immunocytochemistry

To stain for Tau-1, 2D neurons were fixed in 4% paraformaldehyde (PFA) (Merck) in sucrose (Fluka) at 37°C for 30 min, quenched in 50 mM ammonium chloride (Merck) at room temperature (RT) for 15 min, and permeabilized with 0.1% Triton X-100 (Sigma) at RT for 3 – 5 min. For 3D cultures, times were in general tripled, i.e., 1.5 h fixation, 45 min quenching and 10-15 min permeabilization on a shaker. For microtubule and F-actin labeling, neurons were simultaneously fixed and permeabilized in PHEM buffer [60 mM Pipes (Sigma), 25 mM HEPES (GIBCO), 5 mM EGTA (Sigma), and 1 mM Magnesium Chloride (Sigma)] containing 0.25% glutaraldehyde (EMS), 3.7% PFA in sucrose, and 0.1% Triton X-100 as previously described (Smith, 1994; Witte et al., 2008) for 20 min and quenched as above for 30 min. For 3D cultures cells were fixed and permeabilized for at least 1 h and quenched for 1.5 h. The neurons were then blocked at RT for 1 h (2D) or 3 h (3D) in a solution containing 2% fetal bovine serum (Invitrogen), 2% bovine serum albumin (Sigma), and 0.2% fish gelatin (Sigma) dissolved in phosphate-buffered saline (PBS) (AppliChem). Subsequently, cells were incubated with primary antibodies diluted in 10% blocking solution. The primary antibodies used were: mouse-anti-Tau-1 (Clone PC1C6; 1:1,000; Millipore) and rabbit-anti-β tubulin III (clone Tuj 1) (1:1.000; Sigma). Secondary antibodies used were AlexaFluor568-conjugated anti-mouse (1:1000, Invitrogen; for Tau-1) and AlexaFluor488-conjugated anti-rabbit (1:1000; Invitrogen; for Tuj 1). For visualization of F-actin and microtubules: 4 U/ml rhodamine-coupled phalloidin (stored as a 200 U/ml methanol stock solution at −20°C) (Invitrogen) or 100 nmol/μl of Atto647N-Phalloidin (stored as 20 nmol/ml methanol stock solution at −20°C) (Sigma) and AlexaFluor594-conjugated anti-tubulin β III (Tuj 1) (1:500; Biolegend) or AlexaFluor488-conjugated anti-tubulin β III (Mouse IgG2a, Clone: Tuj 1; 1:1000; Biolegend) were used. For the 2D cultures cells were incubated with the primary antibodies at RT for 1 h and for 3D overnight shaking and washed with PBS. The secondary antibodies were added at RT for 1 h. After being washed, the coverslips were mounted with Fluoromount (Sigma) or ProLong Diamond Antifade Mountant (Invitrogen) for STED microscopy. The gels were washed several times in PBS throughout the next day and the secondary antibodies were added at RT/with shaking ON. The next day, the gels were washed several times and kept in PBS with 0.02% sodium azide (Sigma) for imaging and stored at 4°C for several months.

Drug Treatments

Drug treatments were carried out at 2 h post-plating for 2D or at the addition of N2 for 3D cultures (around 20-30 min after the drop of collagen mixture was placed on the dish).

Stock solution of the actin depolymerization drug cytochalasin D (CytoD) (Enzo) was dissolved in DMSO (Roth) at 20 mM and applied to neuronal cultures at final concentrations of 1 μM. For the inhibition of myosin-II activity, blebbistatin (Blebb) (Sigma) was dissolved in DMSO at 20 mM and applied to neuronal cultures at final concentrations from 0.5 to 2 μM.

EDTA treatment was carried out using stock solution of 500 mM EDTA (AppliChem) directly for a final concentration in cell medium of 2 mM (Benoit et al., 2000).

Antibody inhibition of β1-integrin was used from antibody [P5D2] (ab24693) (Abcam) at a final concentration of 20 μg/ml.

In Utero Electroporation and Slice Culture

In utero electroporation was performed according to Saito and Nakatsuji (Saito and Nakatsuji, 2001) with minor modifications. Briefly, timed pregnant mice with E13.5 embryos were anaesthetized with isoflurane, and uterine horns were exposed. Embryos were injected with 2-4 μL pTub-alpha1-mGFP DNA solution [2 μg/μL, 0.3 mg/mL Fast Green (Sigma)] into the lateral left ventricle through the uterine membrane. The hippocampi were electroporated by holding the head of each embryo between tweezer-style circular electrodes (5 mm diameter, Harvard Apparatus). Five pulses (33 V, 50 ms (ms) duration, interval 600 ms, unipolar) were delivered with a square-wave generator (ECM 830; Harvard Apparatus). The uterine horns were returned into the abdominal cavity, the wall and skin were sutured, and the embryos were allowed to resume normal development. For pain medication, the mother was given Temgesic (0.03 mg/kg s.c. injection, Invidior). Baytril (1.5% in 100 μl s.c., Bayer) was used as an antibiotic.

The organotypic cultures were generated according to Stoppini et al. (1991) with minor alterations. After 3 days, the embryos' transfected hippocampi were dissected and sectioned with a thickness of 300 μm on a McIlwain tissue slicer. Slices were separated with a pipette in Gey's Balanced Salt Solution (GBSS) (Sigma) enriched with glucose (5 mg/mL) and placed on a standing insert of Hydrophilic Polytetrafluoroethylene (PTFE) (Millicell, Millipore). The excess of GBSS was removed and the insert was placed in 50 mm glass bottom dishes (FluoroDish, WPI) with 1 mL of culture media. The culture media consisted of 50% MEM supplemented with 0.25x Glutamax (GIBCO) and 20 mM HEPES, 25% horse serum, 25% Hank's Balanced Salt Solution (HBSS) (GIBCO), 0.5% Penicillin-Streptomycin-Glutamine (GIBCO), 0.5% Glucose. After 1 h of settlement, the slices were ready to be imaged.

Plasmids

pmNeonGreen-N1 and -C1 were purchased from Gentaur Europe BVBA (Kampenhout, Belgium). mNeonGreen coding sequence was amplified by PCR using forward 5′-CGAGGATCCCGCCACCATGGTGAGCAAGGGCGAGGAG and reverse

5′-CGAGCGGCCGCCTATTACTTGTACAGCTCGTCCATGCCCATC primers. mNeonGreen was inserted in place of mCherry in pEB3-mCherry (Flynn et al., 2012) as a BamHI/NotI fragment. The plasmid was made by Charlotte Coles.

pCAG-mGFP was a gift from Connie Cepko (Addgene plasmid # 14757) (Matsuda and Cepko, 2007).

Lifeact-RFPruby used here was described by Riedl et al. (2010).

pTub-alpha1-mtGFP plasmid was generated in two steps: a rat Tub-alpha1-promoter was excised from a pTub-alpha-1-DsRED (Addgene plasmid #17707) by digestion with NdeI/BamHI, and cloned into a pCMV-Zsgreen-N1 vector where the CMV promoter was removed by digestion with AseI/BglII. All these complementary restriction sites were destroyed in the resulting pTub-alpha1-ZsGreen plasmid. Second, ZsGreen in pTub-alpha1-ZsGreen was removed by XhoI/NotI digestion and replaced with a mGFP obtained by XhoI/NotI digestion of a pCAG-mGFP (Plasmid #14757, Addgene) to generate a pTub-alpha1-mtGFP plasmid. The plasmid was made by Sebastián Dupraz and is deposited at Addgene #138981.

Imaging Fixed Neurons

The image acquisition of fixed neurons in 2D was performed with an AxioObserver.D1(Zeiss) microscope with the objective Plan-Apochromat 40x/1.3 Oil Ph3 M27 (Zeiss). Fixed neurons in 3D were imaged with a LSM710NLO (Zeiss) using the objective LD C-Apochromat 40x/1.1 W Corr M27 (Zeiss). Cells were imaged with a Z stack of 1 μm. The x/y pixel size was 200 nm.

Contraction Assays

Imaging of matrices was performed with an Epi-Scope1-Apotome (Zeiss) with the Objective EC Plan-Neofluar 2.5x/0.075 (Zeiss). Images were processed using the tile scan function of the Zen software – Blue Edition (Zeiss).

DIC Videos

All conditions were imaged simultaneously per experiment and only in one plane. The long-term experiments were done with an Epi-Scope1-Apotome (Zeiss) with the Objective Plan-Apochromat 20x/0.8 (Zeiss). The dishes were kept alive in an Ibidi chamber (heating system 8 with CO_2 incubation unit I). The environmental conditions were 37°C and 5% CO_2. Images were acquired every 5 min for 48 h. For growth cone imaging an objective Plan-Apochromat 63x/1.4 Oil DIC M27 (Zeiss) was used. The videos were only acquired in one plane every 5 s for 10 min.

STED Imaging

Fixed neurons were imaged in a Leica SP8/STED 3X with the HC PL APO 93X/1.30 GLYC motCORR – STED WHITE objective (Leica). The growth cones were imaged in their full volume with x/y pixel size of 25 nm and z spacing of 80 nm. A pulsed 775 nm laser was used for depletion. The STED power used was 40% and the 3X module at 45%.

Cytoskeleton Dynamics

Transfected neurons of each condition were imaged every 3 s for 5 min. The x/y pixel size was 130 nm and 2 stacks were acquired with 500 nm spacing. Neurons in the gels were carefully selected not to be too close to the glass bottom. Images were acquired in a Leica SP8 with the HC PL APO 63x/1.30 Glyc CORR CS2 objective (Leica). The environmental conditions were 37°C and 5% CO_2.

Slice Imaging

The hippocampal slices from electroporated embryos were imaged in a DeltaVision Core Setup (GE Healthcare, Life Sciences) with an incubation (37°C and 5% CO_2).

Reflection/Confocal Traction Force Microscopy

Neurons transfected with pTub-alpha1-mGFP and meningeal fibroblasts transfected with pCAG-mGFP were imaged with the Leica SP8 with a HC PL APO 63x/1.30 Glyc CORR CS2 objective (Leica), equipped with a pre-equilibrated environmental chamber (37°C, 5% CO2). The voxel size was 120x120x600 nm^3. Cells were imaged for 1 h every 2 min. Backscattered light from WLL irradiation at 670 nm was collected on a hybrid detector (HyD, Leica), enabling the visualization of collagen fibers. Afterward, cells were killed using the phototoxicity of the WLL at 400 nm and 488 nm simultaneously at maximum power focused on the cell body for 10 min, and a reference image with relaxed cell forces was acquired.

Figures

The panels were prepared in the ImageJ2 distribution Fiji with the plugin FigureJ designed by Jerome Mutterer (CNRS) (Mutterer and Zinck, 2013). The graphs were generated using GraphPad Prism version 7.0c for MacOSX, GraphPad Software, La Jolla California USA, https://www.graphpad.com/. The figures were assembled together in Adobe Illustrator CS5 version 15.1.0 for MacOSX, Adobe Systems Incorporated, https://www.adobe.com/.

QUANTIFICATION AND STATISTICAL ANALYSIS

Length of the Longest Neurite

For 2D neurons, processes were quantified using the semi-automatic tracing tool NeuronJ (Meijering et al., 2004) on the ImageJ2 (Rueden et al., 2017) distribution of Fiji (Schindelin et al., 2012). For 3D neurons, length was quantified with Imaris v 8.2, FL package, (Bitplane AG software, available at https://imaris.oxinst.com).

Branching

Branching was quantified as the mean number of branches per cell, with no-order discrimination. The branching results represent the total number of branches per neuron.

Polarity Stages and Tau-1 Positive Cells

For polarity assessment, at least 20 fields of view were acquired for every condition in each experiment. To assess the degree of polarization, cells were classified as "stage 1" "stage 2" or "stage 3" neurons (Bradke and Dotti, 1997; Tahirovic and Bradke, 2009). We analyzed the progression of the cells through the cell stages using an ordinal logistic regression model. Cell stages are represented as ordinal and time as continuous variables.

For the Tau-1 positive cells, neurons were classified as "Tau-1^{+}" or "Tau-1^{-}." We analyzed the ratio of Tau-1^{+} and Tau-1^{-} cells using a generalized linear model with binomial distribution. The model is similar to a binomial logistic regression model but it can account for confounding effects. Cell stages are represented as categorical and the time as continuous variables. We correct for a confounding effect of the three individual experiments. We use R version 3.3.3 (Team, 2008) for the statistical analysis with the MASS package (v7.3.45) (Venables et al., 2002) and the multcomp package (v1.4.6) (Hothorn et al., 2008).

Long-term Videos of Growth Dynamics

The videos were first transformed in a Z-projection (minimum intensity for the DIC and maximum intensity for the slice imaging) in order to have an overview of the areas where the neurite grew. In each, a segmented line of 5 pixels of thickness traces a path where there was growth. Four Kymographs were generated for each cell analyzed, using a macro tool on Fiji written by Volker Baecker at Montpellier RIO Imaging (http://www.mri.cnrs.fr/fr). Speed of retraction and extensions were calculated from the kymographs. Length and number of events were also taken from the kymographs.

Growth Cone Morphology by STED Imaging

All images were deconvolved with Huygens Professional version 17.04 with the STED module (Scientific Volume Imaging, the Netherlands, https://svi.nl/) using the CMLE algorithm, with a signal over noise ratio (SNR) estimate of 5 and 50 iterations. Surface masks were created semi-automatically for both actin and microtubules with Imaris v 8.2 and all parameters analyzed were extracted from the surfaces. The microtubule volume was calculated relative to the volume of the actin surface. The partition of the growth cone was analyzed by manually observing the STED growth cone images for actin arcs (partition) or no actin arcs (no partition) (Dupraz et al., 2019).

Growth Cone Active Area in DIC Imaging

A minimum intensity projection was created from time-lapse recordings in order to visualize the more dynamic areas, appearing darker. The contours of the growth cone were traced manually in order to measure the total growth cone area. The dynamic region was selected with a threshold based on intensity. This measured area was normalized to the total area of the growth cone.

Cytoskeletal Dynamics

All images were deconvolved with Huygens Professional version 17.04, using the CMLE algorithm, with SNR: 15 and 50 iterations. A maximum intensity projection of the 2 planes was created for quantification. Four Kymographs were generated for each growth cone analyzed. In these kymographs, the microtubule growing speed and the actin retrograde flow were quantified. For the quantification of the microtubule intensity to the leading edge, the entire time-lapses were projected. A line scan from the edge of the growth cone to the axonal shaft was traced and the fluorescence intensity of the EB3 signal was normalized to the maximum intensity of each growth cone.

Fiber Perturbation Frequency

Using the DIC videos from the adhesion removal assays with anti-β1-integrin and EDTA incubation, 10 line-scans of 1.2 μm width and 30 μm length determined the areas to generate kymographs around the analyzed cells, as described above. The perturbation of the fiber was visible by a deviation of the position of the fiber through the time axis. These perturbations were counted in total and divided by the time of the videos, 48 h. Experiments were repeated at least 3 times.

Rheometry

After mixing the collagen gel with 10x DMEM and 5.5% sodium carbonate, the gel precursor was quickly loaded on an Anton Paar MCR 301 rheometer equipped with a 20 mm plate-plate geometry and metal floor, precooled to 4°C and in a humidified chamber. The

probe was quickly lowered to measuring position (monitoring the gel precursor forming a crown around the geometry while lowering the probe manually). The temperature was kept at 4°C for 200 s before quickly ramping up to 37°C, mimicking the transfer to a cell culture incubator, while monitoring the storage and loss moduli with 1 Hz oscillations at 4% strain. The gelation time (as defined by crossing over of the storage and loss moduli) happened approximately 380 s after setting the temperature to 37°C. A plateau was reached after 540 s, at which point gelation was considered complete. The measurement was kept for an additional 660 s (total 20 min) to confirm that a steady state has been reached, and the stiffness of the gel was defined as the final storage modulus value. The measurement was repeated 3 times.

Traction Force Microscopy Measurements

The time-lapse images acquired with confocal/reflection microscopy were analyzed using an open-source integrated traction force microscopy analysis library (https://github.com/nbroguiere/TFM) in MATLAB 2017 (MathWorks Inc, Natick, Massachusetts, USA). The shear modulus used was the one experimentally measured for our collagen gels (200 Pa), and the Poisson ratio was taken as zero as a first approximation for small deformations – even though for large deformations the Poisson ratio of collagen can change dramatically and increase up to > 5. Average pressure data was extracted in user defined box, based on visual recognition of growth cones and fibroblast processes, as an average of the pressure values in elements contained in the box weighted by the surface area of the associated mesh elements.

Statistics

All plotted values are expressed as means plus/minus standard error of the mean (SEM). All experiments were performed independently at least three times. Specific numbers can be found in the figure legends. N indicates number of experiments, n indicates number of single cells. If not otherwise indicated, two group comparisons were performed by using a Students t test, more than two group comparisons were done using the one-way ANOVA followed by Tukey's multiple comparisons test in GraphPad Prism version 7.0c for MacOSX.